

Ultrafast Photoluminescence from Thermal Radiation

Leon Oleschko
supervised by Peter Baum
22.10.2025
Draft

Projekt Praktikum
Universität Konstanz

Available at www.github.com/leoole100/projekt-praktikum.

1 Introduction

2 Numerical Model

The ultrafast thermal dynamics are modeled using a simplified two-temperature approach. An excitation pulse $P_{\text{exc}}(t)$ generates an absorbed power density $P_V(t) = P_{\text{exc}}(t)/V$ over the material's volume V . This input energy raises the electron temperature T_e , governed by the electronic heat capacity $C_e(T_e)$. Subsequently, the electrons cool via electron-phonon coupling with a relaxation time τ to the lattice at a constant temperature T_l .

This process is described by the ordinary differential equation:

$$\frac{dT_e(t)}{dt} = \frac{P_V(t)}{C_e(T_e)} - \frac{T_e(t) - T_l}{\tau}. \quad (1)$$

A numerical solution based on used excitation parameters (an absorbed energy density of $U_{\text{abs}} = 2 \text{ GJ/m}^3$ spread in a Gaussian pulse with a full width at half maximum (FWHM) of 250 fs) is provided. We utilize the electronic heat capacity function from [1] and the $\tau = 250 \text{ fs}$ coupling time for graphite [2]. The resulting time evolution is shown in Figure 1.

The spectral radiance L_λ emitted at each time step can be calculated using Planck's law:

$$L_\lambda(\lambda, T) = \epsilon(\lambda) \frac{2hc^2}{\lambda^5} \frac{1}{\exp(hc/\lambda k_B T) - 1}. \quad (2)$$

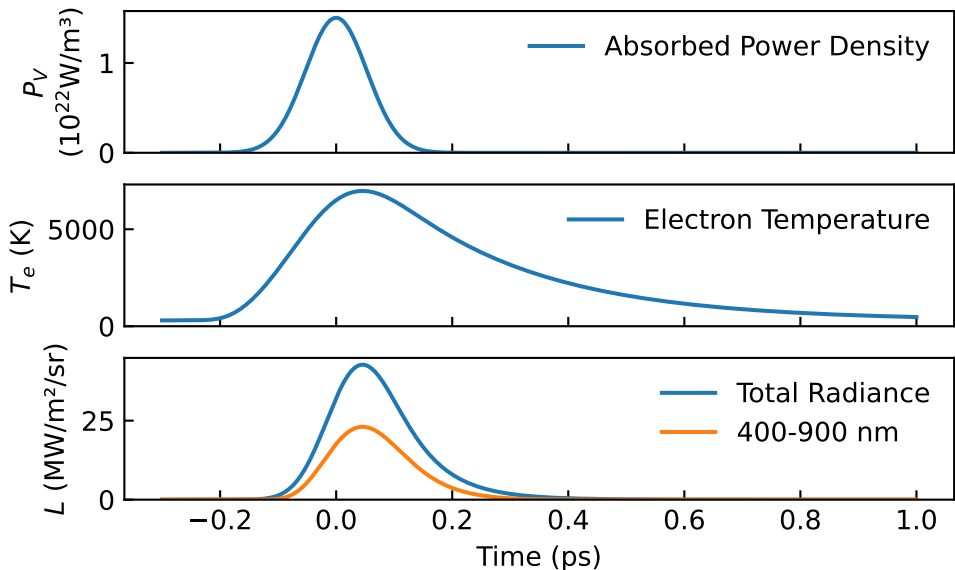


Figure 1 Time evolution of the absorbed power density $P_V(t)$, the electron temperature $T_e(t)$ and the total integrated radiance $L(t)$, calculated using the two-temperature model (Eq. 1). The calculation assumes an absorbed energy density of $U_{\text{abs}} = 2 \times 10^9 \text{ J/m}^3$ over a FWHM pulse with $t = 250 \text{ fs}$ and an electron-phonon coupling time of $\tau = 250 \text{ fs}$ (for graphite). The rapid temperature rise and subsequent decay illustrate the ultra-fast nature of the thermal dynamics.

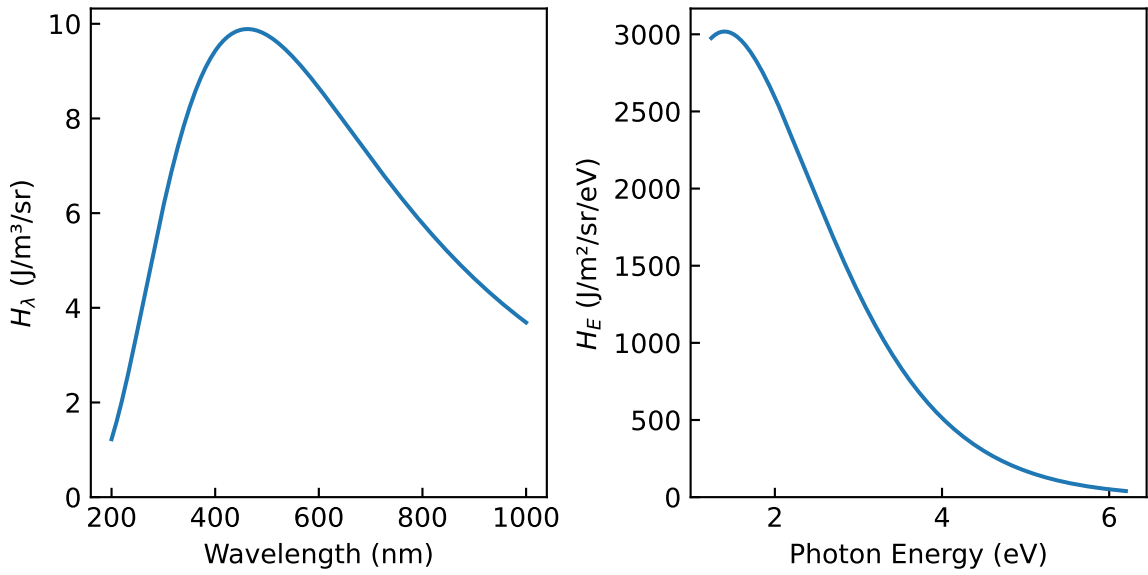


Figure 2 Model spectrum $H_\lambda(\lambda)$ (time-integrated spectral radiance) calculated from the time evolution shown in Figure 1. The spectrum represents the total signal expected to be recorded by a time-integrating detector. Both shown over the wavelength and the photon energy.

The electron gas emissivity ϵ is assumed to be unity, a common approximation for graphite [3]. The resulting time evolution of the total radiance $L = \int L_\lambda(\lambda, T) d\lambda$ and the radiance in a spectral range relevant for common detectors are also presented in Figure 1.

The experimentally measurable spectrum, $H_\lambda(\lambda)$, is defined as the time-integrated spectral radiance:

$$H_\lambda(\lambda) = \int L_\lambda(\lambda, T_e(t)) dt. \quad (3)$$

This is shown in Figure 2. It is noted that this spectrum can alternatively be visualized as a function of photon energy $E = hc/\lambda$. For direct comparison with the spectrometer output, however, we opt for the wavelength representation in this report.

2.1 Sensitivity

This model is employed to study the sensitivity of the resulting spectrum to changes in the defining physical and experimental parameters. The spectrum is calculated while systematically sweeping each parameter, as detailed in Figure 3.

The analysis reveals that the spectrum changes considerably with variations in the absorbed energy density U_{abs} and the electron-phonon coupling time τ . This high sensitivity emphasizes the critical importance of precisely controlling these two parameters. In contrast, changes in the excitation pulse duration t and the lattice temperature T_l do not significantly alter the resulting spectrum.

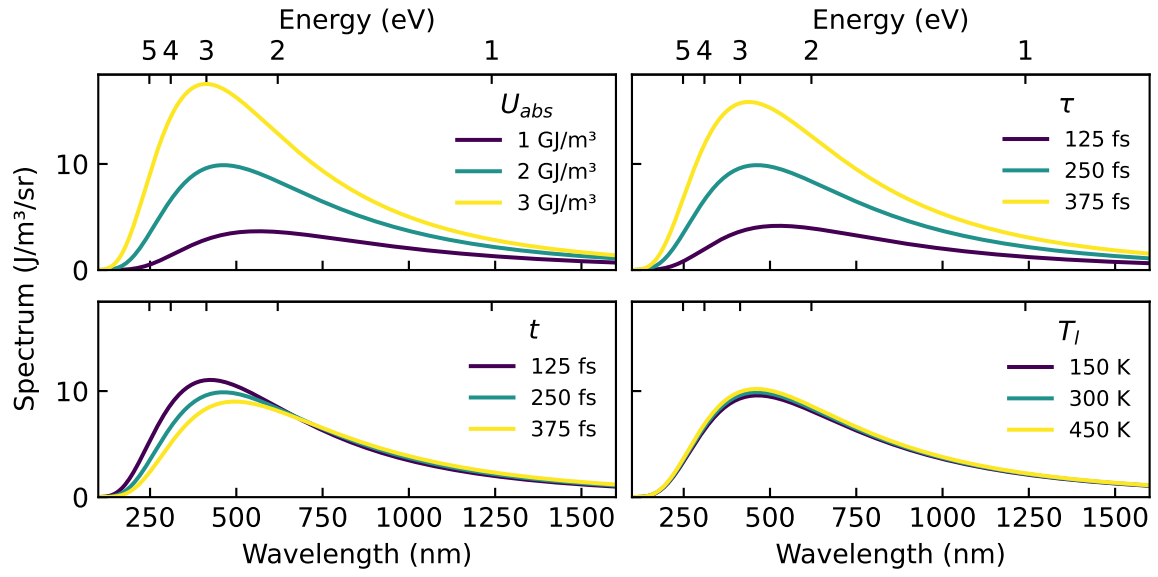


Figure 3 Sensitivity analysis of the calculated spectrum $H_\lambda(\lambda)$ to changes in key model parameters. The results demonstrate that the absorbed energy density U_{abs} and the electron-phonon coupling time τ are the dominant factors influencing the spectral shape and total emission. Conversely, variations in the pulse duration t and the lattice temperature T_l show only marginal impact.

The dependence of the total emitted power $\int H_\lambda(\lambda)d\lambda$ on the absorbed energy density is shown in more detail in [Figure 4](#) for both the total emission and the spectral range relevant for the detector.

Crucially, the scaling is not described by a simple power law. This non-trivial behavior is a direct consequence of the changing electronic heat capacity $C_e(T_e)$ at high temperatures.

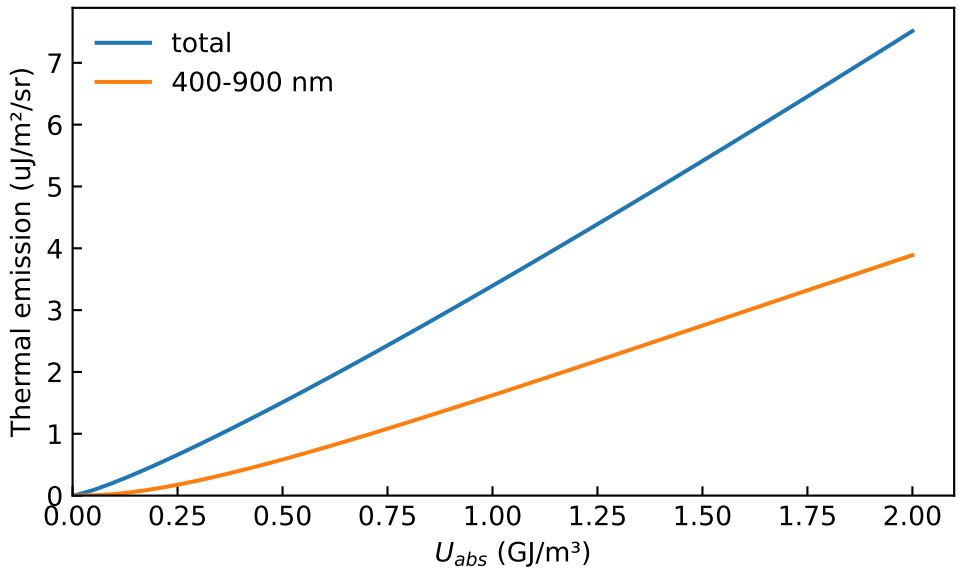


Figure 4 Scaling behavior of the emitted thermal radiation as a function of the absorbed energy density U_{abs} . The scaling is shown for both the total integrated spectrum ($\int H_\lambda d\lambda$) and the radiance within the detector's spectral region. Note the non-power-law dependence, which stems from the temperature-dependent electronic heat capacity $C_e(T_e)$.

3 Experimental Setup

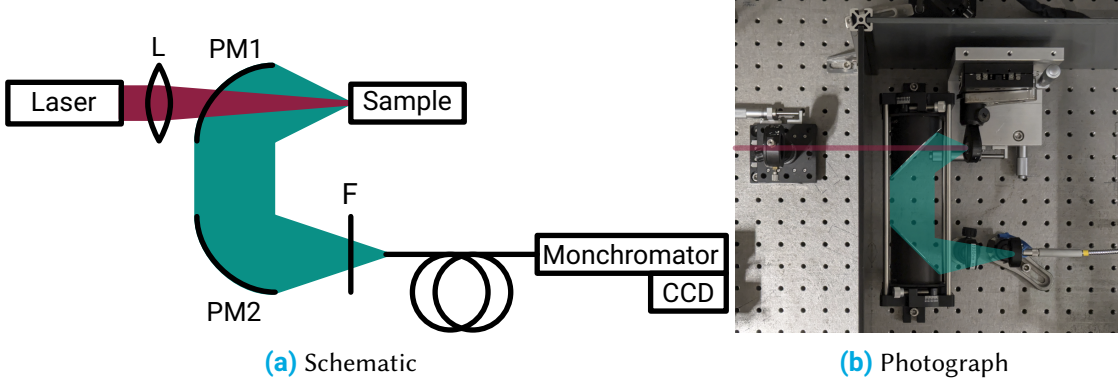


Figure 5 Experimental setup used to measure thermal emission from ultrafast-excited hot electrons. The schematic shows the optical path and key components; the photograph shows the arrangement inside the chamber.

The experimental setup, originally developed by Leon Roob [4], is presented in Figure 5. It is designed to measure broadband thermal emission from hot electrons in graphite using reflective collection optics and a fibre-coupled spectrometer.

The excitation source is a Light Conversion PHAROS PH1-20 at a centre wavelength of 1030 nm, with pulse duration 250 fs (FWHM) and repetition rate 40 kHz. The pulse energy is 7.5 μJ (average power 300 mW). The beam is stabilised in four axes and expanded to a diameter of $D = 5 \text{ mm}$ prior to entering the chamber.

Inside the chamber, a plano-convex lens with focal length $f = 200 \text{ mm}$ focuses the beam onto the sample. The resulting spot diameter is estimated using the standard diffraction approximation $d \approx 4\lambda f/\pi D$ to be $\sim 50 \mu\text{m}$.

The target is a graphite sample mounted on a three-axis translation stage. Thermal emission from the irradiated spot is collected by two off-axis parabolic mirrors (UV-enhanced aluminium). The first mirror (PM1, $f = 50 \text{ mm}$) collimates the emission; the second (PM2, $f = 101 \text{ mm}$) focuses it onto a band-pass filter and into a multimode fibre with a $200 \mu\text{m}$ core (Ocean Optics QP200-2-SR-BX). The magnification is $M = f_{\text{PM2}}/f_{\text{PM1}} \approx 2$, yielding an image spot of $\sim 100 \mu\text{m}$ at the fibre entrance, comfortably within the core, ensuring maximum signal collection.

The fibre feeds an Acton SpectraPro 300i monochromator equipped with a $150 \text{ lines mm}^{-1}$ grating blazed at 500 nm. The dispersed spectrum is detected by an Andor iXon^{EM+} 897 EM-CCD operated in vertical binning mode, effectively acting as a high-sensitivity 1D line detector. Wavelength calibration, performed once following the manufacturer's procedure [4], remained stable throughout the measurements.

For optimal alignment and maximal throughput, the lens, sample, and fibre ferrule are mounted on independent precision translation stages, while PM1 and PM2 are fixed on the common op-

tical axis.

3.1 Noise and detector considerations

Detecting the weak thermal radiation from hot electrons requires careful optimization of the signal-to-noise ratio (SNR). In this setup, detector-related phenomena constitute the dominant noise sources, while laser power fluctuations and mechanical variations are empirically treated as negligible. The underlying EMCCD noise mechanisms are well documented by Andor [5, 6] and standards [7].

Readout Noise (σ_{read}) This is the fundamental noise from charge transfer and A/D conversion. For the present camera, the fit in [Figure 6](#) yields a constant read noise of $\sigma_{\text{read}} = 0.81(12)$ DN, consistent with the manufacturer's specification [8]. Because read noise is applied per readout cycle, utilizing hardware binning (1D line-detector mode) critically minimizes its impact by consolidating signal prior to the single read.

Dark Current Noise (N_{dark}) Thermally generated charge scales with temperature and time, $N_{\text{dark}} \propto \exp(-E/kT) t_{\text{exp}}$. [Figure 6](#) shows the measured dependence; fitting gives an effective activation energy $E = 0.597(4)$ eV. Consequently, with the sensor cooled to -80°C , the dark contribution is confirmed to be negligible for the utilized exposure times.

Clock-Induced Charge (CIC) CIC is created during high-speed clocking. Its contribution scales with the electron multiplication gain; therefore, the *EM gain is disabled* in this work (signal levels are well above the read-noise floor), which keeps CIC negligible [6].

Shot Noise and System Gain (G) Under these optimized conditions (negligible σ_{read} and N_{dark}), the dominant noise term is shot noise. Incident photons create photoelectrons with quantum efficiency η , so $N_e = \eta N_{\text{photons}}$ and, for Poisson statistics, $\text{var}(N_e) = N_e$ [7]. Let G denote the system conversion gain (DN per electron). The measured signal in data numbers (DN) is $S = G N_e$, and the measured variance becomes $\sigma_{\text{meas}}^2 = \sigma_{\text{read}}^2 + G S$. Therefore, a plot of variance vs. mean (the photon-transfer curve) exhibits linearity in the shot-noise regime with a slope equal to G . [Figure 7](#) shows this behaviour; from the slope $G \approx 10$ DN/ e^- can be measured. It is important to note that this procedure determines G but *not* the quantum efficiency η ; it solely quantifies the Data Number-to-electron conversion.

3.2 Data Processing

All raw spectra underwent initial processing by subtracting a dark frame recorded with identical acquisition settings, a procedure which removes the fixed electronic bias and the baseline dark current contribution.

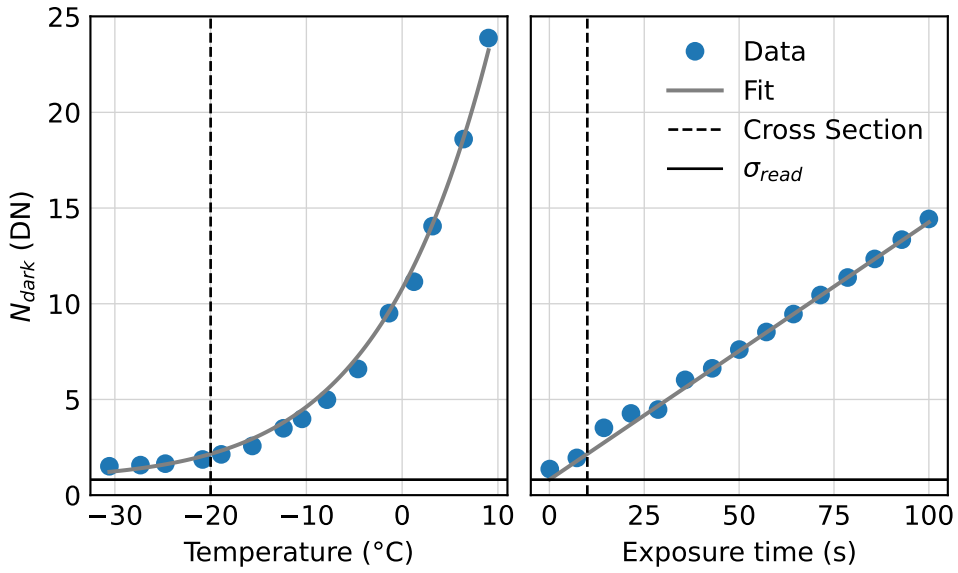


Figure 6 Noise characterization of the EMCCD detector. The plot shows the measured noise versus sensor temperature and exposure time. The fit confirms the read noise $\sigma_{read} = 0.81(12) e^-$ and provides the effective activation energy $E = 0.597(4) \text{ eV}$ for dark current, confirming its negligible impact at the operating temperature of -80°C .

The corrected signal $S(\lambda)$ in Data Numbers (DN) was then converted to spectral power density $P_{\text{meas}}(\lambda)$. This conversion yields the measured signal in energy units (photons/s) and is performed via:

$$P_{\text{meas}}(\lambda) = \frac{S(\lambda)}{G t_{\text{exp}} \Delta \lambda} \frac{hc}{\lambda}, \quad (4)$$

with G being the system conversion gain (DN/e $^-$), t_{exp} the exposure time, and $\Delta\lambda$ the spectral bin width. The final term hc/λ converts the measured signal from electron counts per wavelength bin to the corresponding spectral power density.

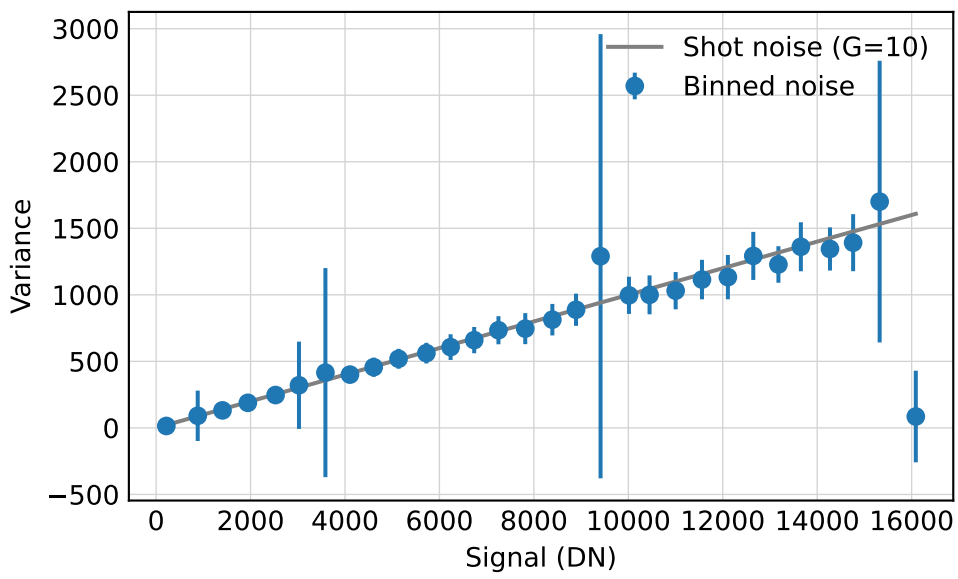


Figure 7 Photon-transfer curve (variance vs. mean signal) demonstrating shot-noise-limited operation under optimized conditions. The linearity of the curve confirms Poisson statistics, and the measured slope yields the system conversion gain, $G \approx 10 \text{ DN}/e^-$.

4 Measurement and Model Validation

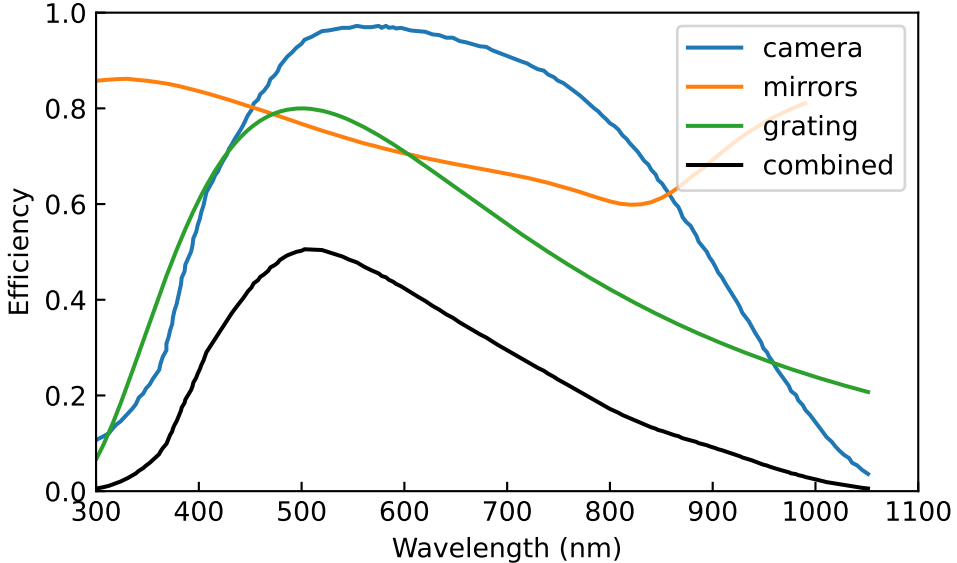


Figure 8 Total spectral efficiency $\eta(\lambda)$ of the detection system, composed of the manufacturer-supplied efficiencies of the camera and mirrors, and the modeled efficiency of the grating. The unknown grating parameter k is determined by fitting the integrated model to the measured spectrum, yielding $k = 1.18$.

Before the model can be compared with the experimental data, the raw spectrum (shown in [Figure 9](#)) must be corrected using the system's spectral calibration curve. This curve, detailed in [Figure 8](#), encapsulates the total wavelength-dependent efficiency $\eta(\lambda)$ of the detection path, encompassing: 1. The manufacturer-supplied quantum efficiency of the EMCCD camera [8]; 2. The measured efficiencies of the reflective optics (mirrors); and 3. The efficiency of the monochromator grating. The grating efficiency, which is the most complex component, is modeled using the method proposed by Barker [9], incorporating a single, unknown parameter k that governs the overall grating performance.

The unknown grating parameter k is determined alongside two other key physical parameters—the absorbed energy density U_{abs} and an overall scaling factor—by simultaneously minimizing the least-squares error between the corrected experimental spectrum and the time-integrated numerical model $H_\lambda(\lambda)$. The results of this optimization are: Grating Parameter: $k = 1.18$; Fitted Absorbed Energy Density: $U_{\text{abs}} = 1.35 \text{ GJ/m}^3$; and Overall Scaling Factor: 0.72×10^{-3} . The corrected experimental spectrum, the numerical model, and the fitted parameters are displayed in [Figure 9](#). While the model demonstrates a strong qualitative agreement with the measured broadband nature of the emission, a precise quantitative fit of the spectral shape proved challenging.

The quantitative mismatch between the model and the measurement necessitates a critical review of the fit parameters and experimental assumptions, specifically regarding two major

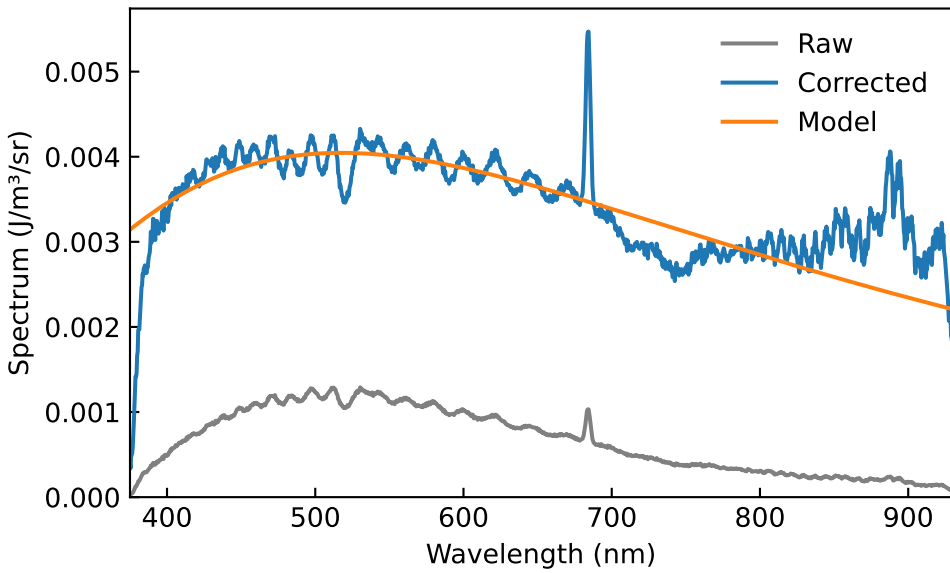


Figure 9 Comparison of the measured spectrum and the fitted numerical model. The figure shows the raw spectrum (in DN), the spectrum corrected using the calibration curve $\eta(\lambda)$, and the resulting fitted model. The strong agreement validates the two-temperature model’s applicability to the ultrafast thermal emission process.

discrepancies. First, the fitting procedure yielded a significant discrepancy in absolute magnitude, requiring a non-physical scaling factor of 0.72×10^{-3} . This indicates that the measured power is nearly three orders of magnitude lower than the absolute radiance predicted by the model. Post-measurement analysis strongly attributed this vast loss factor (in the order of 10^3) to a severe mechanical misalignment in the detection path, specifically a blockage at the fiber coupling into the spectrometer. This suggests the scaling factor primarily reflects a systematic loss in the light collection system, rather than a fundamental deficiency in the physical model’s calculated absolute emission.

Second, the inability to achieve a precise quantitative fit is compounded by spectral contamination. The corrected spectrum contains a broad, uncharacteristic light component (notably around 900 nm) and a distinct peak at 688 nm (a laser harmonic). Given the absence of suitable optical filtering, this contamination is likely composed of residual laser light (fundamental and harmonic) and potentially ambient background light (e.g., neon room light). This spurious signal significantly compromises the comparison with the purely thermal model output.

Regarding the energy input, the fitted absorbed energy density, $U_{\text{abs}} = 1.35 \text{ GJ/m}^3$, is physically plausible as it is lower than the incident energy density, $U_{\text{inc}} = 4.8 \text{ GJ/m}^3$ (based on $P_{\text{avg}} = 300 \text{ mW}$, $f_{\text{rep}} = 40 \text{ kHz}$, $r_{\text{spot}} = 50 \mu\text{m}$, and the absorption depth $d = 200 \text{ nm}$ [10]). This difference can be attributed to surface reflections and scattering losses. The resulting incident fluence is 950 J/m^2 .

5 Discussion and Conclusion

References

- [1] Takeshi Nihira and Tadao Iwata. “Temperature Dependence of Lattice Vibrations and Analysis of the Specific Heat of Graphite”. In: *Physical Review B* 68.13 (Oct. 24, 2003), p. 134305. doi: [10.1103/PhysRevB.68.134305](https://doi.org/10.1103/PhysRevB.68.134305).
- [2] A. Stange, C. Sohrt, L. X. Yang, G. Rohde, K. Janssen, P. Hein, L.-P. Oloff, K. Hanff, K. Rossnagel, and M. Bauer. “Hot Electron Cooling in Graphite: Supercollision versus Hot Phonon Decay”. In: *Physical Review B* 92.18 (Nov. 20, 2015), p. 184303. doi: [10.1103/PhysRevB.92.184303](https://doi.org/10.1103/PhysRevB.92.184303).
- [3] V I Sapritsky. “Black-Body Radiometry”. In: *Metrologia* 32.6 (Dec. 1, 1995), pp. 411–417. ISSN: 0026-1394, 1681-7575. doi: [10.1088/0026-1394/32/6/2](https://doi.org/10.1088/0026-1394/32/6/2).
- [4] Leon Roob. “Thermal Radiation from Ultrafast Hot Electrons in Graphite”. Universität Konstanz, Apr. 29, 2025.
- [5] Dr. Jo Walters. *Sensitivity and Noise of CCD, EMCCD and sCMOS Sensors*. Andor, Apr. 2023.
- [6] Andor. *Establishing Sensitivity in Scientific Cameras*.
- [7] European Machine Vision Association. *Standard for Characterization of Image Sensors and Cameras*. Nov. 29, 2010.
- [8] Andor. *iXonEM+ 897 Manual*.
- [9] P. K. Barker. “Ripple Correction of High-Dispersion IUE Spectra - Blazing Echelles”. In: *The Astronomical Journal* 89 (June 1984), p. 899. ISSN: 00046256. doi: [10.1086/113587](https://doi.org/10.1086/113587).
- [10] T. Smausz, B. Kondász, T. Gera, T. Ajtai, N. Utry, M. Pintér, G. Kiss-Albert, J. Budai, Z. Bozóki, G. Szabó, and B. Hopp. “Determination of UV–Visible–NIR Absorption Coefficient of Graphite Bulk Using Direct and Indirect Methods”. In: *Applied Physics A* 123.10 (Oct. 2017), p. 633. ISSN: 0947-8396, 1432-0630. doi: [10.1007/s00339-017-1249-y](https://doi.org/10.1007/s00339-017-1249-y).